
TWO STAGE GNSS OUTLIER DETECTION FOR GRAPH OPTIMIZATION BASED GNSS-RTK/INS/ODOMETER FUSION

Baoshan Song, Penggao Yan, Xiao Xia, Yihan Zhong, Weisong Wen and Li-Ta Hsu

ABSTRACT

Reliable GNSS positioning in complex environments remains a critical challenge due to non-line-of-sight (NLOS) propagation, multipath effects, and frequent signal blockages. These effects can easily introduce large outliers into the raw pseudo-range measurements, which significantly degrade the performance of global navigation satellite system (GNSS) real-time kinematic (RTK) positioning and limit the effectiveness of tightly coupled GNSS-based integrated navigation system. To address this issue, we propose a two-stage outlier detection method and apply the method in a tightly coupled GNSS-RTK, inertial navigation system (INS), and odometer integration based on factor graph optimization (FGO). In the first stage, Doppler measurements are employed to detect pseudo-range outliers in a GNSS-only manner, since Doppler is less sensitive to multipath and NLOS effects compared with pseudo-range, making it a more stable reference for detecting sudden inconsistencies. In the second stage, pre-integrated inertial measurement units (IMU) and odometer constraints are used to generate predicted double-difference pseudo-range measurements, which enable a more refined identification and rejection of remaining outliers. By combining these two complementary stages, the system achieves improved robustness against both gross pseudo-range errors and degraded satellite measuring quality. To ensure real-time feasibility, the high-frequency IMU and odometer measurements are processed through a pre-integration scheme, while a marginalization-based sliding window maintains computational efficiency. The proposed method was validated using several real-world datasets collected in GNSS-challenging conditions. The experimental results demonstrate that the two-stage detection framework significantly reduces the impact of pseudo-range outliers, and leads to improved positioning accuracy and consistency compared with representative baseline approaches. In the deep urban canyon test, the outlier mitigation method has limits the RMSE of GNSS-RTK/INS/odometer fusion from 0.52 m to 0.30 m, with 42.3% improvement.

1 Introduction

Localization is a fundamental requirement for autonomous ground vehicles, such as robotic delivery or patrolling platforms [1]. GNSS provides continuous and globally available positioning, navigation, and timing (PNT) services, making it the backbone of outdoor navigation [2]. In particular, GNSS real-time kinematic (RTK), based on double differenced (DD) carrier-phase measurements, can achieve centimeter-level positioning accuracy after resolving carrier-phase ambiguities, which is sufficient for high-precision applications such as automated surveying, precision agriculture, and autonomous vehicle navigation [3]. However, double differenced GNSS measurements are still vulnerable to gross errors caused by multipath, signal blockage, or environmental reflections, especially in urban canyons, dense forests, tunnels, or other complex environments [4]. These gross measurement errors, commonly referred to as outliers, not only degrade standalone GNSS positioning performance but also propagate into any navigation system that relies on GNSS, including loosely or tightly coupled integrated navigation with an IMU or an odometer [5]. In such systems, even occasional GNSS outliers can introduce significant biases in velocity, heading, or position estimates, potentially causing divergence or long-term drift.

A GNSS receiver typically takes pseudo-range, carrier-phase, and Doppler measurements as the primary inputs [6]. Each of these observables may suffer from abnormal deviations due to multipath effects, atmospheric disturbances, satellite hardware faults, or receiver-related issues [7, 8]. Pseudo-range measurements are easily affected by the reflected signal which could lead to large ranging bias. Together, carrier-phase measurements are sensitive to abrupt discontinuities, and such abnormal jumps are commonly referred to as cycle slips, which represent a special form of

outlier [9]. Accurately identifying and handling these faulty measurements is crucial for ensuring the reliability of downstream PNT applications. The research on GNSS outlier detection and mitigation has last for decades. From the perspective of input sources, existing outlier detection and mitigation methods can be broadly divided into GNSS-only and sensor-aided strategies.

GNSS-only outlier mitigation is general but limited to geometric information statistics. In this work, we first focus on the outlier mitigation for the generated measurements after signal processing. In this phase, GNSS-only approaches typically include pre-processing and robust state estimation. The pre-processing method relies on the physical models, aiming to flag outliers before the data are passed into the estimator. The fundamental idea is to recognize part of the measurements using consensus check on single or multiple kinds of GNSS measurements. The effectiveness of this step strongly depends on the information source used to form the prediction. Traditional GNSS-only pre-processing methods exploit internal redundancy of the measurements, such as pseudo-range checks [10], carrier-phase combination tests [11], or Doppler cross-validation [12]. These methods are attractive because they do not require external sensors, but they often suffer from degraded performance in challenging environments with limited satellite visibility or highly correlated errors. More recently, advanced estimation methods and machine learning-based techniques have been introduced to enrich the prediction model. For instance, [13] utilizes an autoregressive integrated moving average (ARIMA) model together with a multilayer perceptron (MLP) to generate pseudo-GNSS time series, thereby enabling the identification of outliers that deviate from learned patterns. The robust estimation often exploits residual analysis or statistical consistency checks tied to a particular estimation framework. For example, [14] employs a particle filter to detect pseudo-range and Doppler outliers by analyzing deviations in the measurement innovation sequence. Such methods can be accurate in some applications, but their performance is tightly related to the assumed system model and estimation algorithm, making them less flexible across different application scenarios.

Sensor-aided outlier mitigation is feasible but relies on accurate reference. In addition to GNSS-only approaches, sensor-aided methods, leveraging information from motion sensors or perception maps to assist outlier detection, have open a new window for outlier detection and mitigation in GNSS challenging environments. For example, a 3D map is first used in [15] to detect the NLOS measurements. However, the 3D map could cost much time and money to generate, making it to difficult to maintain. [16] employs the innovation sequence from a tightly coupled GNSS/IMU filter to mitigate pseudo-range outliers, where the IMU serves as a short-term reference. [17] proposes a robust iterated cubature Kalman filter to minimize the impact of GNSS outliers under NLOS and multipath conditions in GNSS/INS fusion. While this strategy can be effective, it also introduces new challenges: IMU measurements are subject to intrinsic errors such as bias, scale factor, and noise, which vary between devices and can drift over time. If these parameters are not properly calibrated or estimated online, the predicted GNSS measurement will be inaccurate, which in turn may lead to false alarms or missed detections. As a common sensor on the ground vehicle, an odometer could provide stable velocity measurements during operation in environments. Similar to IMU, an odometer could provide high-frequency measurements to resume the vehicle motion in two dimensions [5]. Nevertheless, it is still not employed to enhance GNSS measurement quality checking.

The objective of this work is to address these limitations observed in both GNSS-only and sensor-aided strategies, particularly in terms of detection accuracy and robustness under real-world conditions. To this end, we propose a two-stage GNSS outlier mitigation framework. In the first stage, raw GNSS measurements undergo consistency checks and redundancy tests to capture obvious anomalies in a GNSS-only fashion. In the second stage, pre-integrated IMU and odometer measurements are incorporated into a joint GNSS quality-checking module, where they serve as physically consistent references over short time intervals. By combining the complementary strengths of GNSS redundancy and inertial pre-integration, the proposed method is capable of detecting both abrupt and subtle outliers more reliably, even in challenging environments such as urban canyons or tunnels. We also apply this GNSS outlier detection and mitigation method to a FGO-based GNSS-RTK/INS/odometer fusion system, demonstrating that our hybrid design offers a pathway toward more dependable GNSS-based navigation solutions in autonomous ground vehicles. The contributions of this work can be summarized as follows:

1. **Two-stage GNSS outlier detection framework:** A practical two-stage approach is proposed to enhance GNSS measurement reliability. The first stage employs Doppler measurements to detect pseudo-range outliers using GNSS-only information, while the second stage refines the detection using predicted pseudo-range from pre-integrated IMU and odometer measurements.
2. **Application in a tightly coupled GNSS-RTK/INS/odometer system:** The outlier detection is embedded in a factor graph optimization framework that jointly estimates navigation states and IMU-odometer parameters. This enables the system to maintain high positioning accuracy and consistency in challenging environments where GNSS signals may be degraded.
3. **Experimental validation and real-world applicability:** Extensive simulations and real-world experiments demonstrate the effectiveness of the proposed method under various GNSS-challenging scenarios. The

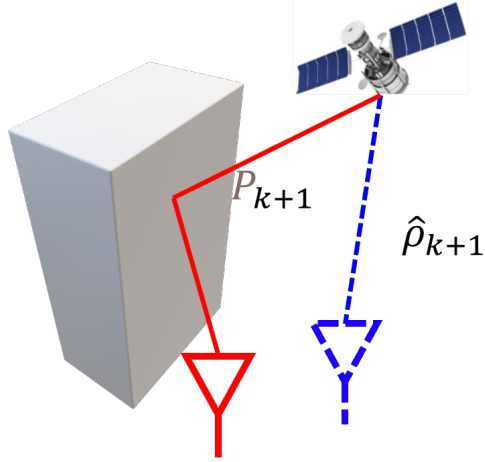


Figure 1: Basic principle of the proposed GNSS outlier detection method, where real red shape and line denote the receiver position estimated using pseudo-range measurements and the pseudo-range affected by multi-path signal, the dashed blue shape and line denotes the predicted position and the predicted range measurement using Doppler or IMU/odometer measurements.

framework is robust to limited satellite geometry and measurement outliers, and it provides a foundation for practical deployment in autonomous ground vehicles.

2 GNSS Outlier Detection

The basic principle of the proposed two-stage GNSS outlier mitigation framework is illustrated in **Figure 1**. The input of the system consists of GNSS measurements from base station and rover station (including pseudo-range and Doppler measurements), IMU measurements (angular velocity and acceleration), and odometer measurements (angular and linear velocity). Based on the GNSS input, the first stage performs a GNSS-only measurement pre-processing. Then the second stage employ pre-integrated IMU and odometer measurements to refine the GNSS measurements. Finally, a factor graph optimization based RTK/INS/odometer integrated navigation system is employed to evaluate the effectiveness of the proposed GNSS outlier mitigation method.

2.1 GNSS-only outlier detection

Since the pseudo-range is prone to large biases caused by multipath and NLOS receptions, it is often unreliable as a direct constraint in degraded environments. In contrast, Doppler measurements, which represent the carrier frequency shift induced by the relative motion between the satellite and the receiver, are much less sensitive to multipath and environmental reflections. This is because Doppler is generally derived from the time derivative of the carrier phase, and therefore does not accumulate the absolute bias caused by excess path delays. Moreover, Doppler provides a smooth and continuous estimate of the range rate with decimeter-per-second level accuracy, even when the corresponding pseudo-range is corrupted. As a result, the Doppler measurement can serve as a reliable reference to detect inconsistencies: if the temporal difference of pseudo-ranges does not agree with the Doppler-predicted range rate, it indicates that the pseudo-range is contaminated by gross errors. In this way, Doppler acts as a stable reference to validate and filter pseudo-range observations in real-time. Given a Doppler measurement $\hat{D}_{GNSS,k}$ at epoch k , we can get the predicted time-differenced range $\delta\rho_{k+1,dopp}^k$:

$$\delta\rho_{k+1,dopp}^k = \hat{D}_{GNSS,k} \cdot \delta t_{k+1}^k \quad (1)$$

where $\hat{D}_{GNSS,k}$ denotes the Doppler measurement at epoch k ; δt_{k+1}^k is the interval from measurements k to $k + 1$. At the same time, we consider the pseudo-range at the last epoch is healthy and compute the time-differenced pseudo-range,

$$\delta\hat{P}_{k+1}^k = \hat{P}_{k+1} - \hat{P}_k \quad (2)$$

Then we can compare the predicted range and measured range with:

$$\kappa_{k+1,dopp} = |\delta\rho_{k+1,dopp}^k - \delta\hat{P}_{k+1}^k| \quad (3)$$

This will be used at the first stage of the outlier detection method in Section 2.3.

2.2 IMU and odometer aided outlier detection

In this section, both the IMU and the odometer measurements are integrated to predict the true GNSS measurements. To lighten the computing load, in the pre-processing part, measurement input is down sampled to a certain frequency and both IMU and odometer are preprocessed by pre-integration methods. Subsequently, pre-integration results from IMU and odometer could be fused in the GNSS outlier mitigation and the factor graph module.

2.2.1 IMU pre-integration model

In this paper, the IMU provides high-frequency acceleration and angular velocity observations affected by bias and other noise. To utilize the IMU measurements, pre-integration model is adopted to construct relative pose constraints between two keyframes. Since the theory of IMU pre-integration is mature, we refer to the details in [18].

2.2.2 Odometer pre-integration model

Note that both the form and frequency of observations from the odometer are similar to the IMU. To reduce the computing load, a modified pre-integration model is derived to cope with odometer measurements in this section. Firstly, the raw measurements from the odometer mechanics model are given by:

$$\begin{aligned}\omega^b &= (1 + s_\omega) \cdot \hat{\omega}^b + \varepsilon_\omega \\ v^b &= (1 + s_v) \cdot \hat{v}^b + \varepsilon_v \\ \dot{s}_v &= \varepsilon_{s_v} \\ \dot{s}_\omega &= \varepsilon_{s_\omega}\end{aligned}\tag{4}$$

where v^b and ω^b denote the true linear and angular velocity in three directions respectively; \hat{v}^b and $\hat{\omega}^b$ denote the raw linear and angular velocity measurements in three directions separately; ε_v , ε_ω , ε_{s_v} and ε_{s_ω} are random noises, which are modeled as white noises. Notably, the odometer only provides forward linear velocity and bearing angular velocity in one direction. In our modified pre-integration model, the plane action model is adopted in this paper to provide pseudo three-dimension observations, since robots with the odometer should always stay and move on a ground. To limit the drift of the odometer, the corresponding scalar s_v and s_ω are augmented to the state vector and modeled as a random walk.

Then, the continuous integral model of odometer measurements from epoch k to $k+1$ is given by:

$$\begin{aligned}\alpha_{odo} &= R_w^{b_k} \int_k^{k+1} R_{b_t}^w ((1 + s_v) \hat{v}^b + \varepsilon_v) dt \\ \gamma_{odo} &= \int_k^{k+1} \frac{1}{2} \Omega' ((1 + s_\omega) \hat{\omega}^b + \varepsilon_\omega) q_t^{b_k} dt\end{aligned}\tag{5}$$

where α_{odo} and γ_{odo} denote pre-integrated odometer measurements; Ω' denote the quaternion right-hand multiplier in [19]. Together with the integral of measurements, the propagation model of corresponding covariance matrix is given by disturbance theory in the $\delta X = F\delta X + G\varepsilon$ form:

$$\begin{bmatrix} \delta\dot{\alpha}_{odo,k} \\ \delta\dot{\gamma}_{odo,k} \\ \delta\dot{s}_{v,k} \\ \delta\dot{s}_{\omega,k} \end{bmatrix} = \begin{bmatrix} \mathbf{0} & -[\mathbf{R}_{b,k}^w ((1 + s_v) \hat{v}_k^b \times)] & \mathbf{R}_{b,k}^w \hat{v}_k^b & \mathbf{0} \\ \mathbf{0} & -[(1 + s_\omega) \hat{\omega}_k^b \times] & \mathbf{0} & \hat{\omega}_k^b \\ \mathbf{0} & \mathbf{0} & 0 & 0 \\ \mathbf{0} & \mathbf{0} & 0 & 0 \end{bmatrix} \begin{bmatrix} \delta\alpha_{odo,k} \\ \delta\gamma_{odo,k} \\ \delta s_{v,k} \\ \delta s_{\omega,k} \end{bmatrix} + \begin{bmatrix} \mathbf{R}_{b,k}^w & \mathbf{0} & \mathbf{0} & \mathbf{0} \\ \mathbf{0} & \mathbf{I} & \mathbf{0} & \mathbf{0} \\ \mathbf{0} & \mathbf{0} & 1 & 0 \\ \mathbf{0} & \mathbf{0} & 0 & 1 \end{bmatrix} \begin{bmatrix} \varepsilon_v \\ \varepsilon_\omega \\ \varepsilon_{s_v} \\ \varepsilon_{s_\omega} \end{bmatrix}\tag{6}$$

Subsequently, by the first-order approximation, the update of pre-integrated covariance P^k from measurements i to $i+1$ is given by:

$$P_{i+1}^k = (I + F_i \delta t_i)(P_i^k + G_i Q_i G_i^T)(I + F_i \delta t_i)^T\tag{7}$$

where δt_i is the interval from measurements i to $i+1$; Q_i is the covariance matrix of $\varepsilon_{v,i}$, $\varepsilon_{\omega,i}$, $\varepsilon_{s_v,i}$ and $\varepsilon_{s_\omega,i}$ from measurements i .

In the INS/odometer-aided outlier mitigation part, an outlier mitigation model is applied, after which pseudo-range measuring outliers are detected and downweighted. To make the process clear, we rewrite the details for pseudo-range outlier detection here and it is similar for carrier-phase. First, we predict the robot position at epoch $k+1$ with the pre-integration results from IMU and the modified pre-integration results from odometer separately. Then we apply the predicted position into GNSS model to get the predicted double differenced (DD) range $\nabla\Delta\rho_{ins}$ and $\nabla\Delta\rho_{odo}$. Since

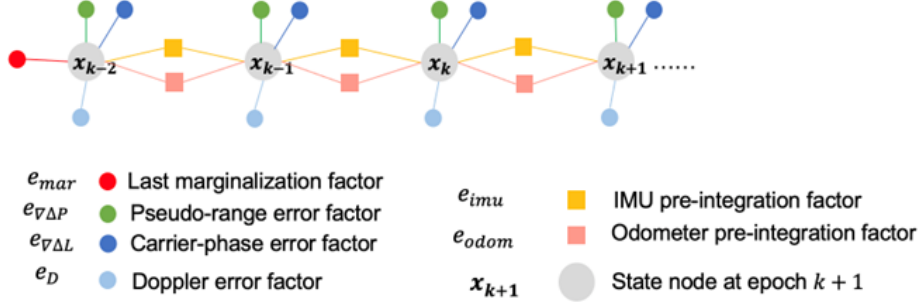


Figure 2: GNSS/INS/odometer integrated factor graph structure overview, including state nodes and factor edges composed by marginalization, double differenced pseudo-range, double differenced carrier-phase, Doppler, IMU integral and odometer integral measurements.

the IMU and odometer can provide high-precision relative position prediction, we get the single difference DD range between previous epoch k and current epoch $k + 1$ as below (only demonstrate the IMU based model):

$$\delta\rho_{k+1,ins}^k = \nabla\Delta\rho_{k+1,ins} - \nabla\Delta\rho_{k,ins} \quad (8)$$

At the same time, we reuse the single difference DD pseudo-range from GNSS receivers.

$$\delta\hat{P}_{k+1,gnss}^k = \nabla\Delta\hat{P}_{k+1,gnss} - \nabla\Delta\hat{P}_{k,gnss} \quad (9)$$

Finally, the detection value κ_{k+1} can be estimated by the difference between $\delta\rho_{k+1,ins}^k$ and $\delta\hat{P}_{k+1,gnss}^k$.

$$\kappa_{k+1,ins} = |\delta\rho_{k+1,ins}^k - \delta\hat{P}_{k+1,gnss}^k| \quad (10)$$

If $\kappa_{k+1,ins}$ is larger than the preset threshold up to sign, the GNSS DD measurement will be marked as an outlier and down weighted in the following factor graph optimization.

2.3 Two-stage GNSS outlier mitigation algorithm

Based on Section 2.1 and 2.2, we propose a two-stage GNSS outlier detection method to ensure both robustness and consistency of the measurement set. At the first stage, the detection is carried out in a GNSS-only manner: Doppler measurements are utilized to evaluate the temporal consistency of pseudo-range observations. Since Doppler is inherently less sensitive to multipath and NLOS effects compared with pseudo-range, and it reflects the relative dynamics between receiver and satellites, it can serve as a stable reference for identifying suspicious pseudo-range values that deviate significantly from the expected kinematic trend. This stage provides a coarse screening mechanism that quickly removes obvious outliers without relying on additional sensors.

In the second stage, the detection is further refined with the aid of IMU pre-integration and odometer information. By leveraging these inertial and proprioceptive measurements, a set of predicted double-difference pseudo-ranges can be constructed, which embed both the vehicle’s short-term motion constraints and the underlying GNSS geometry. These predicted values offer a physics-based baseline against which the remaining pseudo-range measurements can be cross-validated. Outliers that survive the first stage but remain inconsistent with the predicted double-difference observations are further excluded at this step.

Through this hierarchical detection scheme, the first stage benefits from the availability and stability of Doppler to guard against gross pseudo-range errors, while the second stage introduces a tightly coupled sensor fusion perspective that enforces geometric and kinematic consistency. The combination enables a more reliable identification of pseudo-range outliers than either GNSS-only or sensor-fusion-only methods.

3 Application on Localization

3.1 System State and Factor Graph Structure

In the following parts, the models for integrating screened multi-sensor measurements from pre-processing section, including the double differenced GNSS observations, pre-integrated IMU and odometer measurements, are formulated

to estimate the total robot state X , including n robot state x at one epoch. The factor graph structure is shown in Figure 2. Similar to [19], the states are maintained in the local ENU coordinate system.

$$X = [x_0^T, \quad x_1^T, \quad \dots, \quad x_k^T, \quad \dots, \quad x_{n-1}^T]^T \quad (11)$$

$$x_k = [p_{b,k}^{w,T}, q_{b,k}^{w,T}, v_{b,k}^{w,T}, b_a, b_g, dt_r, s_v, s_\omega]^T \quad (12)$$

where p_b^w is the robot position; q_b^w is the robot attitude quaternion; v_b^w is the robot velocity; b_a and b_g are the bias of IMU; dt_r is the receiver clock drifting rate. The objective function of the proposed RIO method is formulated as follows, including the sum of double differenced pseudo-range residual, double-differenced carrier-phase residual, Doppler residual, IMU residual, odometer residual and marginalization residual

$$X^* = \arg \min_X \sum \left(\|e_{\nabla \Delta P}\|_{\sigma_{\nabla \Delta P}}^2 + \|e_{\nabla \Delta L}\|_{\sigma_{\nabla \Delta L}}^2 + \|e_D\|_{\sigma_D}^2 + \|e_{imu}\|_{\sigma_{imu}}^2 + \|e_{odo}\|_{\sigma_{odo}}^2 + \|e_{mar}\|_{\sigma_{mar}}^2 \right) \quad (13)$$

where σ_{sensor} is the covariance of the sensor residual. Note that the covariance models of double differenced pseudo-range, double differenced carrier-phase measurements and Doppler measurements are given in [19]. The implementation of IMU residual follows [18], more details in derivation can be referred in the reference. Meanwhile, marginalization is adopted in our sliding-window-based optimization process. When the keyframes of GNSS and odometer reach the maximum threshold, marginalization will be performed by Schur complement method [20] and a new prior factor will be added to the graph.

3.2 GNSS Factor

The GNSS factors are based on the methods in our previous paper [5]. Notably, the state in the previous paper is derived in the ECEF frame. Here, we will introduce the position and velocity of the GNSS antenna phase center by transformation from states in the local World-frame to ECEF frame as below:

$$p_g^e = R_n^e R_w^n (p_b^w + R_b^w p_g^b) \quad (14)$$

$$v_g^e = R_n^e R_w^n (v_b^w + [\hat{\omega}_{ib}^b \times] p_g^b) \quad (15)$$

where p_g^e and v_g^e denote the position and velocity of GNSS antenna phase center in the ECEF frame; R_n^e denotes the rotation from ECEF to local navigation frame; R_w^n denotes the rotation from local navigation frame to local world frame; $[\hat{\omega}_{ib}^b \times]$ denotes the skew-symmetric of the IMU gyroscope measurement; p_g^b denotes the GNSS antenna lever-arm from IMU.

Substituting equation (14) (15) into the residual models in [5] leads to the GNSS residuals in this paper:

$$e_{\nabla \Delta P,k} = \nabla \Delta P_{INS,k} - \nabla \Delta \hat{P}_{GNSS,k} \quad (16)$$

$$e_{\nabla \Delta L,k} = \nabla \Delta L_{INS,k} - \nabla \Delta \hat{L}_{GNSS,k} \quad (17)$$

$$e_{D,k} = D_{INS,k} - \hat{D}_{GNSS,k} \quad (18)$$

where $\nabla \Delta P_{INS,k}$, $\nabla \Delta L_{INS,k}$ and $D_{INS,k}$ are the INS derived range and range rate; the variables with hats are the DD or raw GNSS measurements received by the receivers.

3.3 IMU Integral Factor

In this paper, the inertial measurement unit (IMU) provides high-frequency acceleration and angular velocity observations affected by bias and other noise. To utilize the IMU measurements, pre-integration model is adopted to construct relative pose constraints between two keyframes. Since the theory of IMU pre-integration is mature, we refer to the details in [18].

3.4 Odometer Integral Factor

With the pre-integration result from section 2.1.2, when reaching the keyframe of the odometer, the factor formulation will be performed. The residual of the odometer measurement is given by:

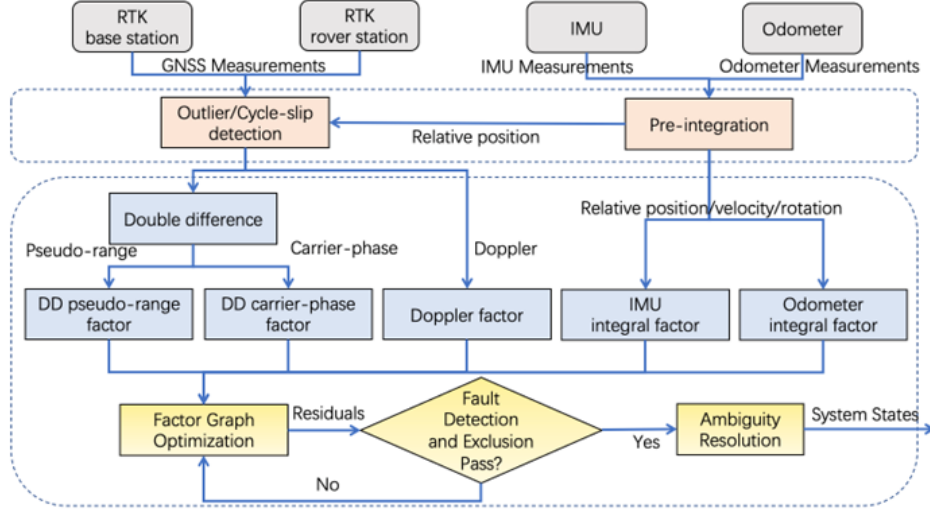


Figure 3: Application of the outlier detection method in an FGO-based GNSS-RTK/INS/odometer fusion system, including four parts: measurement input (grey boxes), the proposed two-stage GNSS outlier detection (pink boxes), factor formulation (blue boxes), optimization and ambiguity resolution (yellow boxes). The pink boxes denote the main contributions of this work.

$$e_{odo,k+1}^k = \begin{bmatrix} \delta\hat{\alpha}_{odo} \\ \delta\hat{\gamma}_{odo} \\ 0 \\ 0 \end{bmatrix} \boxminus \begin{bmatrix} (R_w^{b_k}(p_{b_{k+1}}^w - p_{b_k}^w - J_{s_v,k+1}^p \cdot \delta s_{v,k+1} - J_{s_\omega,k+1}^p \cdot \delta s_{\omega,k+1}) \\ q_w^{b_k} \otimes q_{b_{k+1}}^w \otimes \begin{bmatrix} 0 \\ \frac{1}{2}J_{s_\omega,k+1}^\theta \cdot \delta s_{\omega,k+1}^{-1} \end{bmatrix} \\ s_{v,k+1} - s_{v,k} \\ s_{\omega,k+1} - s_{\omega,k} \end{bmatrix} \quad (19)$$

where $J_{s_v}^p$, $J_{s_\omega}^p$ and $J_{s_\omega}^\theta$ are the Jacobian matrices on scalar parameters, which considers the first-order approximation on scalar parameters and its impact on the pre-integration process. Specifically, the details of the Jacobian matrixes can be found in Appendix A; The extended minus symbol \boxminus and extended multiplier \otimes are defined in [18].

Together with the definition of states and factors, nonlinear optimization method is employed to solve the factor graph. The Ceres-Solver is adopted here to perform the nonlinear programming (NLP) [19]. After solving the float ambiguity with NLP, the LAMBDA method is employed to re-solve the double-differenced GNSS ambiguity to integer [21]. When the LAMBDA method is successful after consistency check, the fixed solutions in centimeter-level precision will be used as high-precision constraints in the factor graph.

4 Experimental Results

To evaluate the performance of the proposed method in this paper, two experiments are conducted in two urban scenes, including an open-sky garden and a dense urban canyon. During the test, a GNSS receiver u-blox F9P is used to collect raw dual-frequency GNSS measurements at 1 Hz. IMU measurements are collected by a MEMS-IMU Xsens Ti-30 at 400 Hz, and odometer measurements are collected by two-wheel encoders at 25 Hz. Besides, a Velodyne HDL-32 LiDAR is combined with the IMU to provide the ground truth by the LIO-SAM method [22]. To correct the temporal and spatial errors, all the sensors are time-synchronized through Robot Operation System (ROS) and the extrinsic parameters are priorly calibrated. To make the investigation clear, the results were compared by the schemes: 1) RTK via RTKLIB (RTK) [23]; 2) RTK via u-blox F9P (F9P-RTK) [24]; 3) RTK/INS tightly coupled integration based on FGO (RI) [25]; 4) RTK/INS tightly coupled integration based on FGO with INS-aided outlier mitigation (RI-OM); 5) RTK/INS/odometer tightly coupled integration based on FGO (RIO); 6) RTK/INS/odometer tightly coupled integration based on FGO with INS/odometer-aided outlier mitigation (RIO-OM), respectively. During the analysis, positioning performance with/without GNSS outlier mitigation is presented.



Figure 4: The open-sky scene view

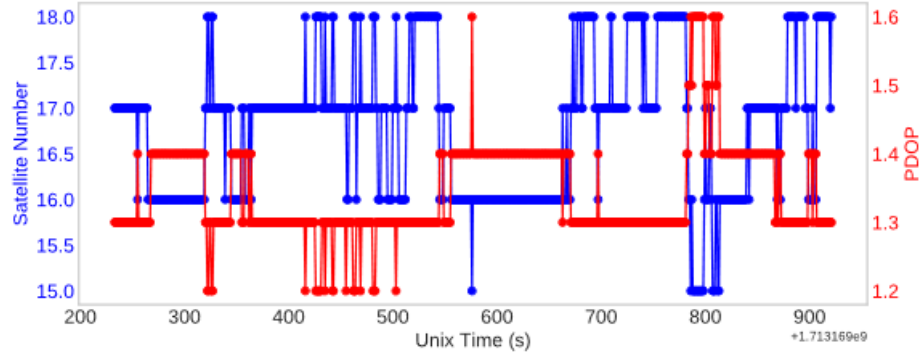


Figure 5: satellite number and PDOP overview, while the average satellite number is 16.78 and the average PDOP is 1.34

4.1 Open-sky test

Figure 4 and 5 illustrate the open-sky testing scene conditions. Figure 6 positioning trajectories of all compared methods. The positioning error of all schemes is showed in Table 1. In this table, MAX means the maximum error; RMSE means the root mean squared error; MAE means the mean of absolute error in 95 percent; all the errors are analyzed with the synthesis of three directions. A mean error of 0.20 m and a RMSE of 0.22 m are obtained by RTK via RTKLIB. Meanwhile, A mean error of 0.17 m and a RMSE of 0.19 m are obtained by F9P-RTK. However, the maximum error of RTK and F9P-RTK reaches 0.49 m and 0.63 m separately. For the other four schemes, they share similar positioning performance while RIO-OM reaches the best place with a maximum error of 0.35 m and a RMSE of 0.18 m. Figure 4 shows the positioning error in horizontal and height directions separately. We can see that the height positioning performance of RTK is poor with a maximum height error larger than 0.4 m. After adding INS, the maximum height error is limited within 0.4 m. With the help of INS/odometer assistance, a smoother trajectory is obtained and the maximum height errors of RIO and RIO-OM are lower than 0.2 m.

4.2 Deep urban canyon test

In this experiment, the scene view and satellite visibility are illustrated in Figure 7 and 8 separately. Performance of all mentioned methods is compared using a deep urban canyon dataset with the trajectory presented in Figure 9. The evaluated positioning error in the deep urban canyon is shown in Table 2. More details in horizontal and height directions can be found in Figure 10. Note that the geometric distribution is worse with the mean satellite number of

Table 1: 3D positioning error statistics of several compared methods in the open-sky test.

3D Error	RTK	F9P-RTK	RI	RI-OM	RIO	RIO-OM
MAX (m)	0.49	0.63	0.39	0.40	0.35	0.35
RMSE (m)	0.22	0.19	0.19	0.18	0.18	0.18
MAE (m)	0.20	0.17	0.17	0.17	0.16	0.16



Figure 6: The open-sky positioning trajectories of all compared methods on the Google Earth software, including Ground-Truth (black), RTK (red), F9P-RTK (pink), RI (yellow), RI-OM (orange), RIO (blue), and RIO-OM (green).



Figure 7: The dense urban canyon testing scene.

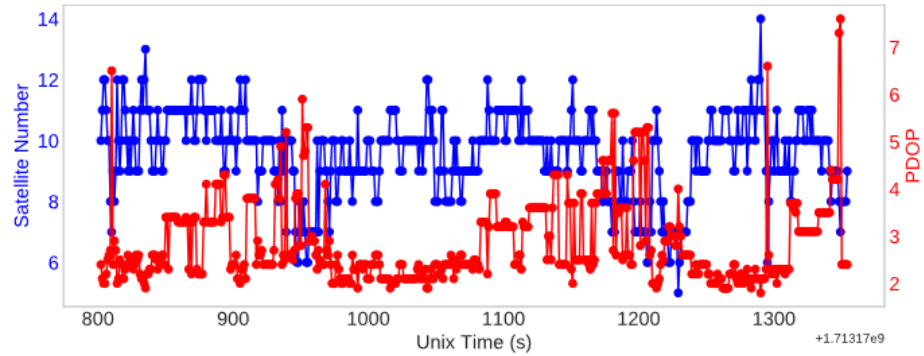


Figure 8: Satellite number and PDOP overview, while the average satellite number is 9.57 and the average PDOP is 2.85.

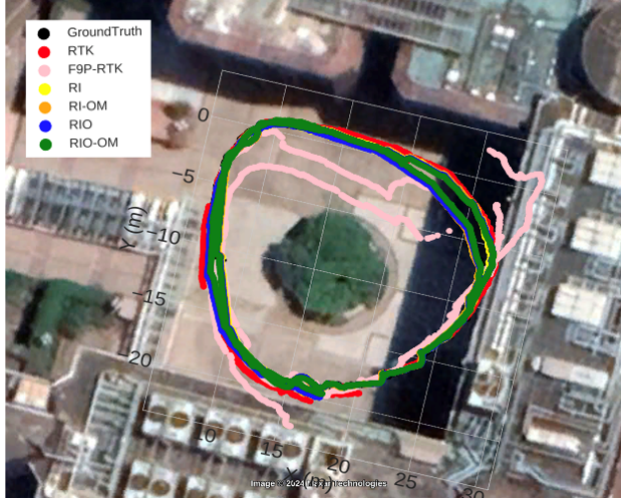


Figure 9: Trajectories of all compared methods on the Google Earth software, including Ground-Truth (black), RTK (red), F9P-RTK (pink), RI (yellow), RI-OM (orange), RIO (blue), and RIO-OM (green).

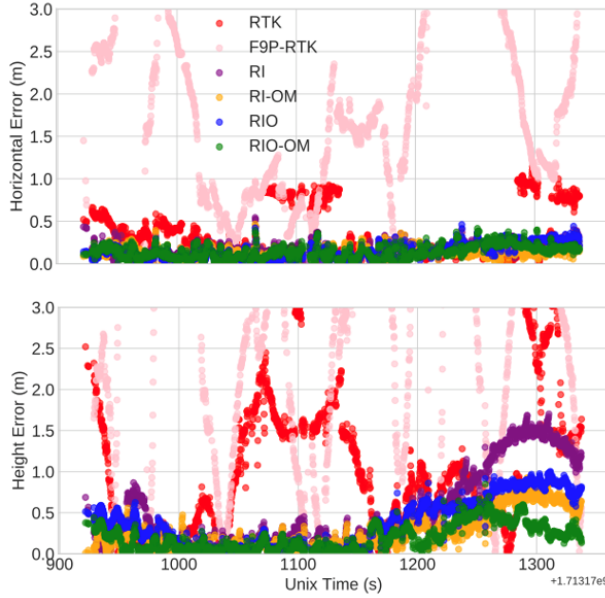


Figure 10: Horizontal and height positioning error of RTK, F9P-RTK, RI, RI-OM, RIO, and RIO-OM

9.57 and PDOP of 2.85, so this scene is challenging for RTK. We can see from Figure 7 that the height positioning error is worse than the horizontal one in RTK scheme. A mean of 1.06 m is obtained using RTK with a RMSE of 1.44 m. Meanwhile, the 3D maximum error reaches 3.86 m. Moreover, the result from F9P-RTK is worse than RTK from RTKLIB. A mean of 3.74 m is obtained by F9P-RTK with a RMSE of 4.71 m. The 3D maximum error of F9P-RTK reaches 11.95 m. The mean error decreases to 0.53 m after applying RI with a RMSE of 0.76 m and a maximum error of 1.72 m. With the help of IMU-aided GNSS outlier mitigation, the mean error of RI-OM decreased to 0.30 m. We can see that the mean error is 0.40 m and the RMSE is 0.52 m for RIO. The reason is that both the IMU and odometer are low-cost sensors and the precision of RTK/INS/odometer integrated positioning highly depends on GNSS measuring quality, which needs the GNSS outlier mitigation. When both odometer measurements and INS/odometer-aided GNSS outlier mitigation are applied, RIO-OM reaches the best precision with a mean error of 0.24 m, a RMSE of 0.30 m and a maximum error of 0.85 m. Compared with RTK and RI, RIO-OM with GNSS outlier mitigation limits the error in all 3D directions with 79.2% and 60.5% improvement in 3D positioning RMSE separately. Compared to RIO, the RIO-OM has limits the RMSE from 0.52 m to 0.30 m, with 42.3% improvement.

Table 2: 3D positioning error statistics of all compared methods in the dense urban canyon test.

3D Error	RTK	F9P-RTK	RI	RI-OM	RIO	RIO-OM
MAX (m)	3.86	11.95	1.72	0.95	1.03	0.85
RMSE (m)	1.44	4.71	0.76	0.38	0.52	0.30
MAE (m)	1.06	3.74	0.53	0.30	0.40	0.24

5 Conclusion

In this paper, we presented a two-stage GNSS outlier detection method and apply it to a tightly coupled GNSS-RTK/INS/odometer system using factor graph optimization. By leveraging Doppler measurements in a GNSS-only first stage and pre-integrated IMU/odometer predictions in a second stage, the method effectively identifies and mitigates pseudo-range outliers, leading to improved positioning accuracy and consistency in challenging environments. Real-world experiments confirmed the robustness and practicality of the approach. Specifically, among the deep urban canyon test, the outlier mitigation method has limits the RMSE of GNSS-RTK/INS/odometer fusion from 0.52 m to 0.30 m, with 42.3% improvement.

Future work will focus on extending the framework to support multi-constellation GNSS signals, evaluating its performance under extreme urban canyon conditions, and exploring adaptive strategies to dynamically adjust the outlier detection thresholds based on the quality of incoming measurements. Further investigation into integrating additional sensors, such as low-cost visual systems, may also enhance robustness without significantly increasing computational complexity.

Acknowledgment

The authors acknowledge the RTKLIB and ROS. The authors also thank UrsRobot Corporation for providing their robot lawnmower for our experiments.

References

- [1] T. G. R. Reid, S. E. Houts, R. Cammarata, G. Mills, S. Agarwal, A. Vora, and G. Pandey, “Localization requirements for autonomous vehicles,” vol. 2, no. 3, pp. 12–02–03–0012.
- [2] P. D. Groves, *Principles of GNSS, inertial, and multisensor integrated navigation systems*. Artech House, second edition ed. OCLC: 880437603.
- [3] W. Wen and L.-T. Hsu, “Towards robust GNSS positioning and real-time kinematic using factor graph optimization,” in *2021 IEEE International Conference on Robotics and Automation (ICRA)*, pp. 5884–5890, IEEE.
- [4] Z. Shen, X. Li, and X. Li, “Advancing high-precision navigation: Leveraging homogeneous sensors in tightly coupled PPP-RTK/IMU integration,” vol. 71, no. 11, pp. 15100–15110. Conference Name: IEEE Transactions on Industrial Electronics.
- [5] X. Li, Z. Qin, Z. Shen, X. Li, Y. Zhou, and B. Song, “A high-precision vehicle navigation system based on tightly coupled PPP-RTK/INS/ odometer integration,” pp. 1–12.
- [6] X. Li, J. Huang, X. Li, Z. Shen, J. Han, L. Li, and B. Wang, “Review of PPP–RTK: achievements, challenges, and opportunities,” vol. 3, no. 1, p. 28.
- [7] N. Sunderhauf and P. Protzel, “Towards robust graphical models for GNSS-based localization in urban environments,” in *International Multi-Conference on Systems, Signals & Devices*, pp. 1–6, IEEE.
- [8] Z. Zhang, J. Zeng, B. Li, and X. He, “Principles, methods and applications of cycle slip detection and repair under complex observation conditions,” vol. 97, no. 5, p. 50.
- [9] F. Huang, W. Wen, H.-F. Ng, and L.-T. Hsu, “LiDAR aided cycle slip detection for GNSS real-time kinematic positioning in urban environments,” in *2022 IEEE 25th International Conference on Intelligent Transportation Systems (ITSC)*, pp. 1572–1578, IEEE.
- [10] Z. Li, D. Wang, and J. Wu, “An inter-frequency cross-validation approach for pseudo-range fault detection in GNSS relative positioning,” vol. 25, no. 16, p. 4908. Publisher: Multidisciplinary Digital Publishing Institute.
- [11] X. Xu, Z. Nie, Z. Wang, and Y. Zhang, “A modified TurboEdit cycle-slip detection and correction method for dual-frequency smartphone GNSS observation,” vol. 20, no. 20, p. 5756.

- [12] L. Icking, F. Ruwisch, and S. Schön, “Doppler as a quality indicator for GNSS-based urban navigation - an evaluation with different receivers and clocks,” in *2020 European Navigation Conference (ENC)*, pp. 1–11.
- [13] J. Guo, Y. Zhou, S. Zhao, and Z. Hu, “A new GNSS outlier mitigation method for GNSS/INS integrated system,” vol. 34, no. 10, p. 105118. Publisher: IOP Publishing.
- [14] S. Zair, S. Le Hégarat-Mascle, and E. Seignez, “Outlier detection in GNSS pseudo-range/doppler measurements for robust localization,” vol. 16, no. 4, p. 580. Publisher: Multidisciplinary Digital Publishing Institute.
- [15] Q. Zhong and P. Groves, “Outlier detection for 3d-mapping-aided GNSS positioning,” pp. 2104–2126.
- [16] R. Sun, J. Wang, Q. Cheng, Y. Mao, and W. Y. Ochieng, “A new IMU-aided multiple GNSS fault detection and exclusion algorithm for integrated navigation in urban environments,” vol. 25, no. 4, p. 147.
- [17] J. Wang, X. Chen, C. Shi, and J. Liu, “Robust m-estimation-based ICKF for GNSS outlier mitigation in GNSS/SINS navigation applications,” vol. 72, pp. 1–17.
- [18] C. Forster, L. Carbone, F. Dellaert, and D. Scaramuzza, “On-manifold preintegration for real-time visual–inertial odometry,” vol. 33, no. 1, pp. 1–21.
- [19] C. Chi, X. Zhang, J. Liu, Y. Sun, Z. Zhang, and X. Zhan, “GICI-LIB: A GNSS/INS/camera integrated navigation library,” vol. 8, no. 12, pp. 7970–7977.
- [20] T. Ando, “Generalized schur complements,” vol. 27, pp. 173–186.
- [21] P. Teunissen, “The lambda method for the GNSS compass,” vol. 41, no. 3.
- [22] T. Shan, B. Englot, D. Meyers, W. Wang, C. Ratti, and D. Rus, “LIO-SAM: Tightly-coupled lidar inertial odometry via smoothing and mapping,” in *2020 IEEE/RSJ International Conference on Intelligent Robots and Systems (IROS)*, pp. 5135–5142, IEEE.
- [23] T. Takasu and A. Yasuda, “Development of the low-cost RTK-GPS receiver with an open source program package RTKLIB,” in *International Symposium on GPS/GNSS*.
- [24] U. Robustelli, M. Cutugno, and G. Pugliano, “Low-cost GNSS and PPP-RTK: Investigating the capabilities of the u-blox ZED-f9p module,” vol. 23, no. 13.
- [25] W. Wen, T. Pfeifer, X. Bai, and L.-T. Hsu, “It is time for factor graph optimization for GNSS/INS integration: Comparison between FGO and EKF.”